nature geoscience

Article

https://doi.org/10.1038/s41561-026-02117-8

Antarctic marine-based ice destabilized when warming outpaces solid-Earth feedbacks

Received: 28 May 2025

Accepted: 2 September 2026

Published online: 20 October 2026

Check for updates

Jan Swierczek-Jereczek[1,2] ✉, Javier Blasco[3], Alexander Robinson[3], Jorge Alvarez-Solas[2] ✉ & Marisa Montoya[1,2]

The Antarctic Ice Sheet is expected to be the largest contributor to sea-level rise over the coming centuries. Previous equilibrium ice-sheet simulations have suggested that this is due to crossing a bifurcation point associated with marine ice-sheet instability. Here we investigate whether sectors vulnerable to this instability can undergo rate-induced tipping, whereby rapid forcing and slow bedrock uplift trigger self-sustained retreat before the bifurcation point is reached. We test this with an ice-sheet model coupled to a glacial isostatic adjustment model, sampling the uncertainty in mantle viscosity. We find that slow bedrock adjustment weakens the stabilizing effect of glacial isostatic adjustment, allowing grounding lines to reach retrograde bed slopes more readily and triggering self-sustained retreat below the bifurcation threshold. Although the West Antarctic Ice Sheet is subject to a bifurcation, it is unlikely to experience rate-induced tipping because of the low mantle viscosity beneath the region. In contrast, the Recovery and Aurora subglacial basins are likely to undergo such a transition even under warming rates lower than those observed today. Depending on mantle viscosity, this mechanism can reduce the critical global mean temperature anomaly by up to 0.5 K, with important implications for the long-term evolution of the Earth system.

The Antarctic Ice Sheet (AIS) contains large sectors that are grounded below sea level: the West Antarctic Ice Sheet (WAIS) and the East Antarctic subglacial basins (EASBs), with volumes above flotation of about 4.3 metres of sea-level equivalent (mSLE) and 19 mSLE, respectively[1–3]. Along many cross sections of these marine-based regions, the bedrock deepens towards the interior of the ice sheet. When the grounding zone retreats on such retrograde slopes, the ice thickness in the grounding zone increases, which in turn, increases the ice outflow through a highly nonlinear relation[4]. The resulting advection ungrounds the ice and promotes further retreat, potentially until a prograde slope is reached again[4,5]. This is commonly referred to as the marine ice-sheet instability (MISI), and the associated self-sustained retreat represents a bifurcation point of the AIS[6–8], beyond which the ice sheet reorganizes to a qualitatively different stable state. MISI drives the high-end projections of the future Antarctic contribution to sea-level rise (SLR), which could reach 4 mSLE by 2300 (ref. 9) and up to 13 mSLE by the end of the millennium[10,11] under high-emissions scenarios. MISI was also simulated in some realizations of lower-emissions scenarios, yielding a few metres of Antarctic SLR contribution by the year 3000 (refs. 10,11).

Over the past decade, several mechanisms have been proposed to provide stabilizing effects on grounding zone retreat, thus conditioning MISI, notably: (1) lateral confinement of the grounding zone through topographic features[12], (2) buttressing by ice shelves[13], (3) higher basal friction in the grounding zone[14], (4) upstream increase

[1]Department of Earth Physics and Astrophysics, Universidad Complutense de Madrid, Madrid, Spain. [2]Geosciences Institute, CSIC-UCM, Madrid, Spain. [3]Alfred Wegener Institute, Helmholtz Centre for Polar and Marine Research, Potsdam, Germany. ✉e-mail: janswier@ucm.es; alvarez.solas@igeo.ucm-csic.es

https://doi.org/10.1038/s41561-026-02117-8

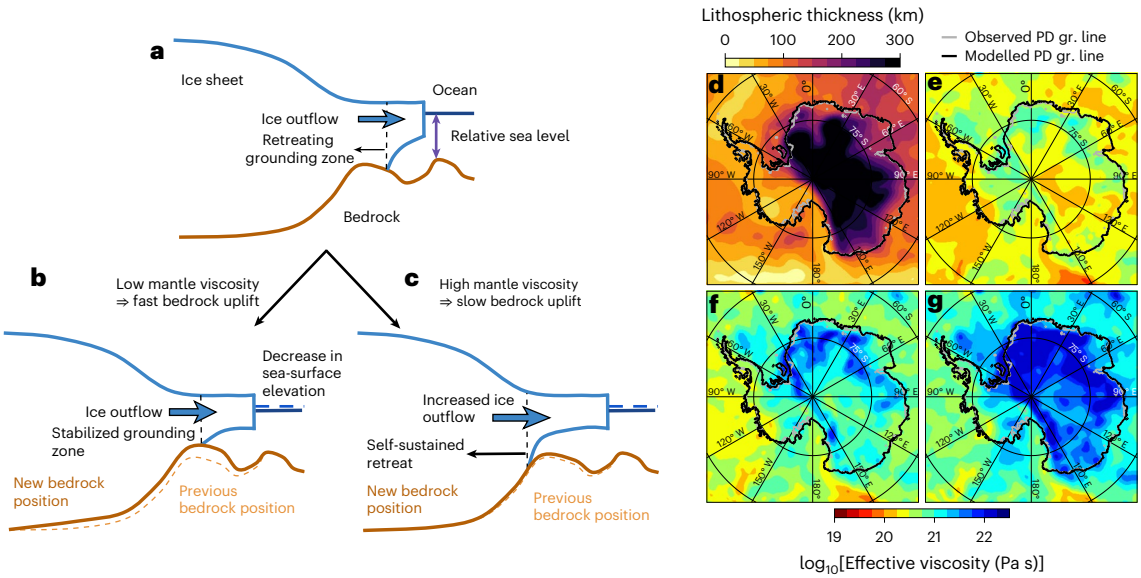


Fig. 1 | R-tipping mechanism controlled by solid-Earth properties of Antarctica. a–c, Schematic representation of the timescale separation between ice dynamics and GIA, which can lead to R-tipping of a marine ice sheet. **b**, For low mantle viscosities and equilibrium experiments, the bedrock uplift is largely synchronous with the grounding zone retreat and prevents reaching retrograde portions of the bed, where MISI can be triggered. **c**, In contrast, high mantle viscosities lead to a delayed bedrock uplift that facilitates the grounding zone retreat into retrograde portions of the bed, thus easing the onset of MISI below the bifurcation point. **d–g**, Lithospheric thickness (**d**) and effective mantle viscosity of Antarctica for -2σ (**e**), 0σ (**f**) and $+2\sigma$ (**g**), as used here[28]. PD gr., present-day grounding.

of precipitation[15] and (5) glacial isostatic adjustment (GIA)[16–19], which is the central mechanism studied here. When ice thins, GIA reduces the relative sea level (that is, the difference between the sea-surface and bedrock elevations) via bedrock uplift and, to a lesser extent, via a reduction of the gravitational pull of the ice sheet on the ocean (Fig. 1a–c). Via the flotation criterion, this provides a strong negative feedback on ice retreat, both on palaeoclimatic timescales[20,21] and over short future projection horizons[22,23]. The timescale governing the viscous bedrock uplift is largely determined by the mantle viscosity, which is assumed homogeneous in most GIA models used for ice-sheet simulations. In reality, it varies laterally by up to a few orders of magnitude between the old East Antarctic craton and the West Antarctic rift system[24–28] (Fig. 1e–g). Thus, the timescale separation between grounding zone retreat and the stabilizing GIA response is particularly small in the west and large in the east. Although this relative pattern is robust throughout the literature, the absolute values carry large uncertainties[24–28] that are seldom sampled in ice-sheet modelling studies.

Slow bed uplift could lead to R-tipping

In idealized dynamical systems, the transient lag of a stabilizing feedback was shown to allow tipping of a system below the bifurcation point[29]. This only manifests in the case of large forcing rates and is therefore called rate-induced tipping (R-tipping)[30]. To date, R-tipping has rarely been studied in tipping elements of the Earth system, despite anthropogenic warming rates that are unprecedented for at least the last 150 kyr (ref. 31). R-tipping of the Atlantic Meridional Overturning Circulation has been identified in an ocean box model[32] and in an ocean model of intermediate complexity[33], although no mechanistic explanation has been provided. A similar analysis was recently applied in a simulation study of the Greenland ice sheet, where R-tipping was, however, found to be negligible[34]. Remarkably, R-tipping of the AIS in a warming climate has not yet been studied. We therefore ask: are the marine-based regions of the AIS subject to R-tipping and is its amplitude controlled by the mantle viscosity?

We hypothesize that a higher upper-mantle viscosity delays the reduction of relative sea level in the grounding zone, particularly for high forcing rates. This facilitates the grounding zone retreat towards retrograde bed portions and the onset of MISI (Fig. 1a–c). This can potentially lead to R-tipping in marine-based regions of the AIS, and thus to large SLR contributions below the bifurcation points. To test this hypothesis, we use Yelmo, a thermo–mechanical 3D ice-sheet model[35], coupled to FastIsostasy, a regional GIA model that can represent the lateral variability of the solid-Earth properties[36]. The error metrics for present-day ice elevation and velocity lie within the Ice Sheet Model Intercomparison for CMIP6 (ISMIP6) ranges (Extended Data Fig. 1); the modelling choices for ice dynamics, basal conditions, sub-shelf melt and surface mass balance are detailed in Methods. We include five viscosity set-ups, obtained by perturbing the nominal 3D viscosity by -2σ, -1σ, 0, $+1\sigma$ and $+2\sigma$, where σ is the 3D standard deviation provided with the estimate[28] (Extended Data Fig. 2). Each perturbed field is then lumped into a 2D effective viscosity (Methods). Figure 1d–g shows the nominal and $\pm2\sigma$ fields, along with the lithospheric thickness, which is fixed for all set-ups because its uncertainty is negligible.

Equilibrium stability of the AIS

To study R-tipping of the AIS, a prior assessment of its bifurcation points is needed. To this end, the AIS is forced by a global mean temperature (GMT) anomaly with respect to the pre-industrial era (1850–1900), beginning at +1.2 K (2015–2025) and converted into regional anomalies of the atmosphere and ocean (Methods). To remain close to equilibrium, an adaptive forcing method applies a very slow warming (0.05 K kyr^{-1}) only if the simulated rate of AIS volume loss is less than one-third of the observed 2000–2017 average[37]; otherwise, the forcing is held constant, thus capturing self-sustained volume loss when bifurcations are crossed.

In addition, for the 0σ case, we branch equilibrium runs off the quasi-equilibrium experiment at each increment of 0.1 K of GMT anomaly, holding the forcing constant over 30 kyr. The resulting equilibrium points lie very close to the curve obtained via adaptive forcing (Fig. 2a), which is therefore a good approximation of the true equilibrium. As extensively shown in a related study[38], the quasi-equilibrium diagram presents many bifurcations, which manifest as vertical lines in the equilibrium diagram. We focus on the five largest ones (purple shadings

https://doi.org/10.1038/s41561-026-02117-8

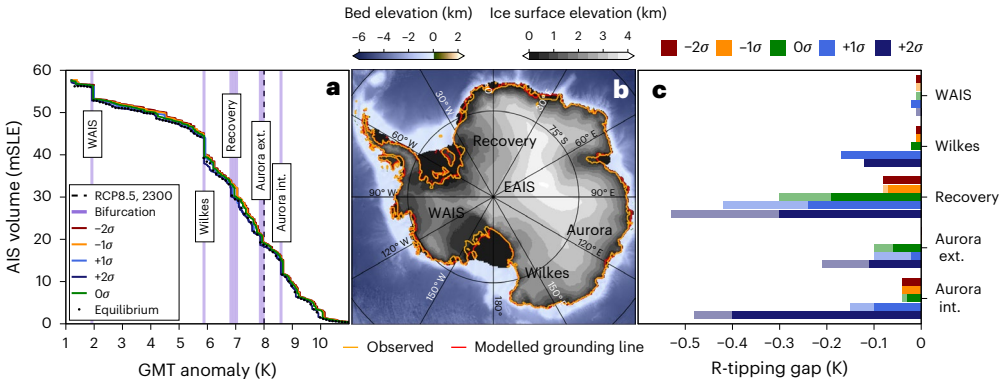


Fig. 2 | Equilibrium and transient tipping behaviour of Antarctica's marine-based regions. a, Quasi-equilibrium diagram of the AIS retreat for various mantle viscosities. Equilibrium runs (black dots) are only branched off for the 0σ case. The Coupled Model Intercomparison Project Phase 5 (CMIP5) mean of GMT anomalies in 2300 under RCP8.5 is shown for comparison (results range from 4 to 13 K, depending on the model)[39]. The five largest bifurcations are highlighted by the purple shadings and are associated with the MISI-driven retreat of the marine-based regions[38]. **b**, Modelled present-day state of Antarctica, closely matching the observed grounding line[53]. **c**, R-tipping gap inferred by comparing step experiments with quasi-equilibrium ones: as the viscosity increases, so does the R-tipping gap, which can reach as much as 0.3 K for the RSB and 0.4 K for the ASB. The bar plots are oriented to the left, because the R-tipping point would be situated to the left of the bifurcation if visualized in the diagram in **a**. The bars in lighter shade represent the cumulative gap with respect to the −2σ case, as described in the discussion. Ext., external; int., internal.

in Fig. 2a), which correspond to the retreat of the WAIS (3.3 mSLE), the Wilkes subglacial basin (WSB, 5 mSLE), the Recovery subglacial basin (RSB, 2.2 mSLE) and the Aurora subglacial basin (ASB). The latter presents two distinct bifurcation points that correspond to the collapse of its external and internal regions (1.7 mSLE and 3.2 mSLE, respectively).

We also perform quasi-equilibrium runs for the ±1σ and ±2σ cases. As viscosity increases, the simulated bifurcation points of the RSB and ASB shift slightly to lower forcing values (Fig. 2a). This is most apparent for the RSB but only amounts to 0.2 K between the −2 and +2σ cases. The bifurcation amplitude behaves similarly: volume loss increases with viscosity. This is clearest for the WSB collapse, which yields 2 mSLE more volume loss for +2σ than for −2σ, whereas other basins differ by much less than 1 mSLE. Overall, sampling the mantle viscosity within realistic ranges only marginally affects the AIS bifurcations.

R-tipping of the East Antarctic subglacial basins

To study the potential for R-tipping, we use the same initial configuration as in the quasi-equilibrium experiments and apply a step of GMT anomaly from 1.2 K to a target value, yielding an infinite forcing rate that maximizes the likelihood of R-tipping. We repeat this for all viscosity cases and for target values spaced by about 0.05 K. The smallest target value that leads to a basin collapse is the R-tipping point. We define its difference from the bifurcation point (assessed separately for each viscosity case) as the R-tipping gap, which quantifies the magnitude of rate-induced effects. Regardless of the mantle viscosity, the R-tipping gap is 0 K for the WAIS. For all other basins, its magnitude increases with the viscosity perturbation, yielding [−0.15, 0] K for the WSB, [−0.3, −0.1] K for the RSB, [−0.1, 0] K for the external ASB and [−0.4, −0.05] K for the internal ASB (Fig. 2c). In other words, R-tipping is absent in the WAIS, marginal in the WSB and external ASB and substantial in the RSB and internal ASB, especially for the +1σ and +2σ viscosity cases. The magnitude of R-tipping is also largest for regions of higher mantle viscosity (Fig. 1e–g). This aligns with the hypothesis formulated above: large timescale separations between ice retreat and GIA response prevent an efficient grounding zone stabilization before retrograde slopes are reached, therefore easing the onset of MISI (Fig. 1a–c).

Because climate mitigation and adaptation strategies are developed based on GMT anomalies on the order of 0.1–1.0 K, some of the R-tipping gaps assessed above could be critical. However, anthropogenic warming rates are not infinite, so step experiments cannot quantify the R-tipping gap for realistic scenarios. We therefore run idealized experiments ramping up the GMT anomaly to a target value that is subsequently held constant to ensure equilibration. For each basin and each viscosity perturbation, we sample target forcings around the bifurcation point and ramp slopes across a wide range that covers the timescales of palaeoclimate and future warming. Figure 3 shows the detailed results for the RSB, while those for the WAIS, WSB and internal ASB are shown in Extended Data Figs. 3, 4 and 5, respectively.

Because the RSB is the first basin to experience substantial R-tipping, we focus on this case to study the underlying mechanisms. In accordance with the step experiments, R-tipping of the RSB increases with the viscosity perturbation (Fig. 3a–e). Furthermore, as expected from our working hypothesis, the magnitude of the R-tipping gap increases with the ramp slope and vanishes for rates that align with the timescale of the viscous bed uplift. Remarkably, the maximum R-tipping gap (−0.3 K) assessed by forcing steps is already reached at warming rates of about 0.07 K per century, which are much smaller than present-day and future ones (Fig. 3c–e). This saturation at high rates arises because the ice sheet acts as a low-pass filter with its own timescale, setting an upper limit on the ice retreat rate and therefore on the timescale separation from the GIA response. Thus, fast forcing rates (>1 K per century) are not a key ingredient for R-tipping of the RSB, because slow rates (<0.1 K per century) already generate a sufficient timescale separation.

By performing a similar ensemble of forcing ramps for the ASB, we observe the same qualitative behaviour (Extended Data Fig. 5): the R-tipping gap is zero for slow ramps and reaches its maximum amplitude for rates that cover the range of present-day and future warming. Realistic scenarios would therefore trigger the largest possible R-tipping gap if the warming amplitude is sufficient. With an ensemble mean of 8 K of GMT anomaly by 2300 and a large associated spread, Representative Concentration Pathway 8.5 (RCP8.5) can provide such forcing[39]. Besides large SLR contributions due to gradual ice retreat, this would overshoot the bifurcations of the WAIS and WSB (about 8 mSLE of self-sustained SLR contribution) and would probably trigger R-tipping of the RSB and ASB (about 7 mSLE of self-sustained SLR contribution; Fig. 2a).

Controls on the R-tipping gap

To understand the mechanism underlying R-tipping, we select the same ramp experiment for various viscosity cases (star markers of Fig. 3a–e). As the viscosity increases, the bed uplift occurs more slowly around the critical part of the RSB grounding zone (orange rectangle, Fig. 3h,i), with a deficit of more than 100 m for +2σ compared with −2σ after several

https://doi.org/10.1038/s41561-026-02117-8

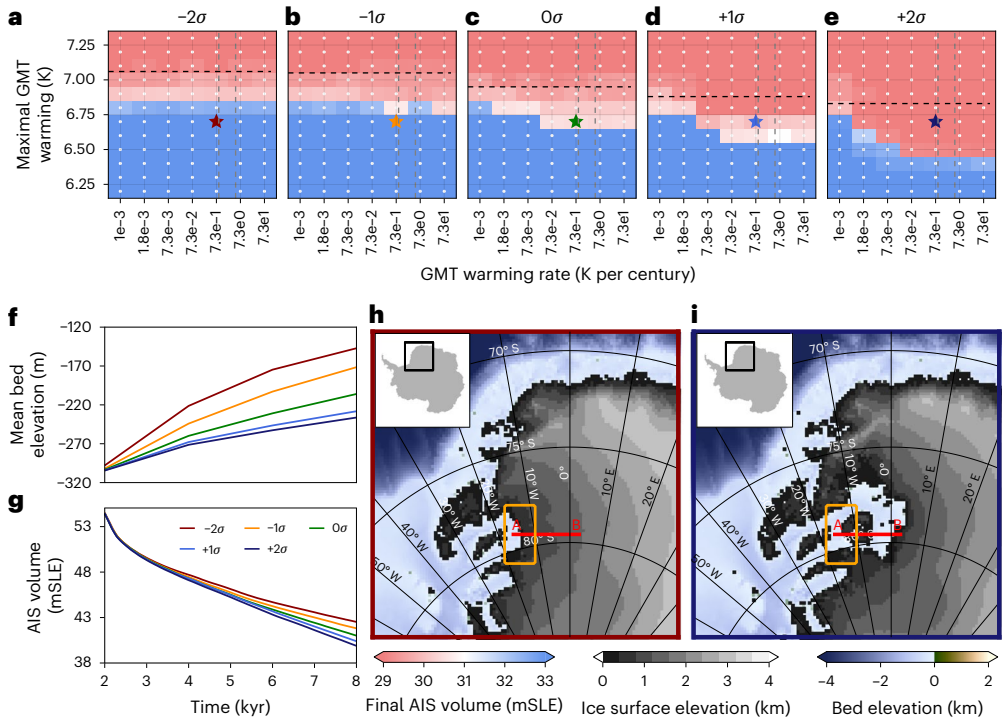


Fig. 3 | R-tipping diagram of the RSB. a–**e**, Final AIS volume above flotation as a function of the maximum rate and amplitude of GMT anomaly (*x* and *y* axes, respectively) for the five upper-mantle viscosity cases: −2*σ* (**a**), −1*σ* (**b**), 0*σ* (**c**), +1*σ* (**d**) and 2*σ* (**e**). The existence of a bifurcation is responsible for the binary behaviour of the final equilibrium AIS volume, which is generally either larger than 32 mSLE (blue) or smaller than 30 mSLE (red), with no values in between. The dashed horizontal line represents the bifurcation point of the RSB and each white dot corresponds to a ramp simulation. The vertical lines represent the mean rate of warming since the pre-industrial era (about 1 K per century) and the highest rate projected until 2300 under RCP8.5 (about 5 K per century). **f**,**g**, Mean bed elevation over the region of interest (**f**) and AIS volume time series (**g**) corresponding to the star markers in **a**–**e**. **h**,**i**, Final RSB configuration for the −2*σ* (**h**, red star in **a**) and the +2*σ* (**i**, blue star in **e**) case with the same ramp forcing. The region of interest is delimited by the orange rectangle and the transect A–B is shown in Fig. 4.

thousand years (Fig. 3f). This prevents an efficient grounding zone stabilization below the bifurcation point, which is manifested by the diverging volume curves (Fig. 3g).

To visualize this effect, we show a transect along the grounding zone retreat direction at the critical time step when the retrograde bed is about to be reached (Fig. 4). As the mantle viscosity increases, bedrock uplift takes place on longer timescales and compensates for the grounding zone retreat less efficiently. Furthermore, the faster uplift of the −2*σ* case creates a pinning point at $x = 80$ km, which prevents ocean melting and further grounding zone retreat into retrograde portions of the bed. In contrast, the bed uplift of the 0*σ* and +2*σ* cases is insufficient for this pinning point to emerge. This highlights that although the bedrock uplift is linear with respect to the ice load[36], its interplay with the bathymetry can give rise to strong nonlinear effects: grounding zone portions below sea level are exposed to much larger basal melt than those above.

We show that higher mantle viscosities can lead to R-tipping and to a lower bifurcation point (for example, the RSB bifurcation point is about 0.2 K lower for +2*σ* compared with −2*σ*; Fig. 2a). The latter could be due either to an actual shift in the stability landscape or to rate-induced effects that persist in quasi-equilibrium simulations, in spite of the small forcing rates. Because the mantle viscosity governs a timescale that is absent from a steady state, we argue that the second hypothesis is more likely, but verifying this would require prohibitively long simulations. In either case, increasing the viscosity perturbation from −2 to +2*σ* reduces the tipping point that is relevant in practice, in addition to the R-tipping gap assessed here. The cumulative gap, computed as the difference between the bifurcation point of the −2*σ* case and the R-tipping point for any of the viscosity cases, can reach as much as 0.5 K for the ASB and RSB, as shown by the lighter shading in Fig. 2c. Furthermore, a related study shows that deactivating GIA lowers all bifurcation points assessed by quasi-equilibrium simulations[38], which effectively provides an upper bound on the R-tipping gap induced by the timescale separation between grounding zone retreat and bedrock uplift.

We also study R-tipping in more detail for the WAIS and WSB, confirming that this effect is largely absent for these regions (Extended Data Figs. 3 and 4). For the WAIS, the lack of R-tipping can be partly attributed to lower uncertainties in the dataset for this region (Extended Data Fig. 2), thus yielding smaller differences in effective viscosity for ±2*σ* (Fig. 1). More importantly, ice thinning and GIA response are relatively small in both regions before the onset of the instability, regardless of the viscosity perturbation. Over the first few thousand years, the mean bedrock uplift around the critical grounding zone reaches only up to 1.5 and 18 m for the WAIS and the WSB, respectively. In comparison, the RSB and ASB yield up to 150 and 170 m of bedrock uplift over the same time span, respectively. The delay of the GIA response is therefore largely irrelevant there. This suggests a more general rule: R-tipping only occurs in transient simulations if the lagging negative feedback shows a substantial magnitude in equilibrium simulations before the onset of the instability. Because the magnitude of bedrock uplift depends on the initial state, accounting for the ongoing isostatic adjustment from the last deglaciation could increase the likelihood of R-tipping in the AIS; this is left for future work.

In East Antarctica, the viscosity dataset we use[28] results in a −2*σ* configuration with viscosities below most literature estimates[25–27], whereas the +2*σ* configuration remains within the typical range.

https://doi.org/10.1038/s41561-026-02117-8

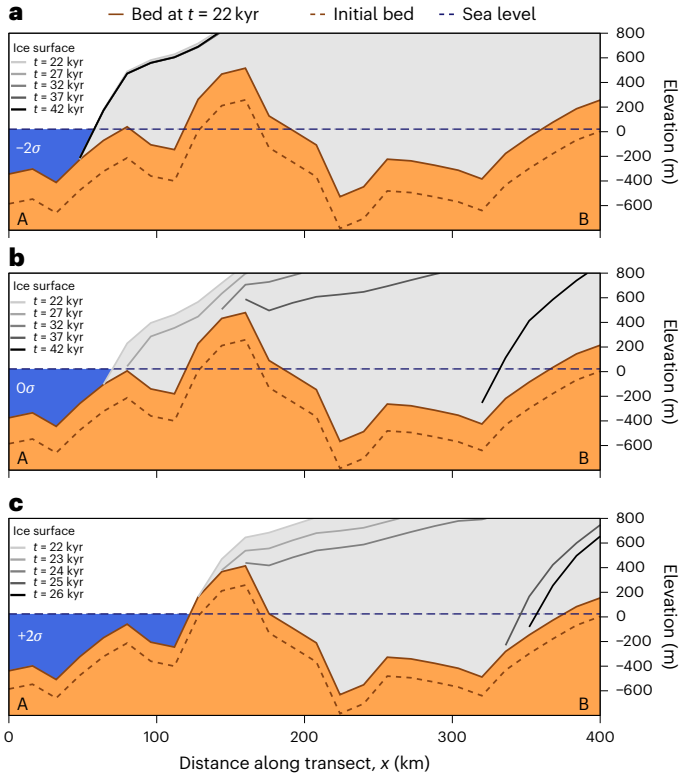


Fig. 4 | Transects of the RSB grounding zone retreat. a–**c**, The transect is shown for simulations with the same forcing but with viscosity perturbations of −2σ (**a**), 0σ (**b**) and +2σ (**c**). The A–B transect location is visualized in Fig. 3h,i. For −2σ, the fast bedrock uplift partially compensates for the retreat and leads to the emergence of a pinning point at x = 80 km that stabilizes the grounding zone. For +2σ, the bedrock uplift is much smaller, which prevents the emergence of a pinning point and leads the grounding zone to reach the retrograde portion of the bed soon after t = 22 kyr, thus entering an unstable regime. t, simulation time. Finally, the nominal viscosity case presents a mixture of both: the bedrock uplift comes close to creating a pinning point and greatly delays the grounding zone retreat but is incapable of stabilizing it before the retrograde slope beginning at x = 160 km is reached.

Table 1 | Summary of autonomous tipping characteristics for the five largest bifurcations of the AIS

Region	ΔV (mSLE)	Δt (yr)	$\dot{s}_{mean}$ (mm yr^{-1})	$\dot{s}_{max}$ (mm yr^{-1})
WAIS	3.3	4,890	0.5	1.8
Wilkes	5.0	10,200	0.4	0.9
Recovery	2.2	12,400	0.1	0.5
Aurora ext.	1.7	6,140	0.2	0.4
Aurora int.	3.2	7,410	0.3	1.0

The confidence interval studied here might therefore be biased towards low viscosities so that the actual magnitude of R-tipping for the WSB, RSB and ASB might be closer to what is simulated for 0 σ, +1σ and +2σ, pointing to a potentially higher vulnerability of these basins than shown here. In West Antarctica, the nominal viscosity is rather large compared with the rest of the literature[25–27,40]. GIA could therefore take place even faster than represented here, which could further reduce the already small likelihood of R-tipping of the WAIS. The viscosity field used here is therefore conservative with respect to our results (marginal R-tipping in the west, substantial R-tipping in the east), supporting their robustness with respect to values commonly found in the literature. Overall, the mantle viscosity appears to be a strong control on R-tipping in marine-based regions of the AIS, which calls for better constraints on this parameter.

Our experiments required a very large number of simulations at 16-km horizontal resolution, amounting to about 100 Myr of model time. This would be computationally intractable for any currently available 3D GIA model but was made possible by FastIsostasy, which is faster by orders of magnitude and was successfully benchmarked against a 3D GIA model[36,41]. Moreover, a quantitatively reliable assessment of MISI requires a good representation of the bathymetry, which demands horizontal resolutions finer than 5 km (ref. 42) and would be computationally prohibitive for such a systematic study. Our findings are therefore first and foremost an attempt to explain why R-tipping is possible in several marine basins, whereas a robust quantification would require a model intercomparison[43]. Moreover, R-tipping of an ice sheet is not necessarily limited to marine-based regions and could arise from timescale separations that are unrelated to GIA. Finally, whereas R-tipping monotonically increases with the rate in our results, some systems show a non-monotonic rate dependency[44,45], particularly when oscillations are present in the system response, as often simulated for ice sheets[46–49].

Implications for future sea-level rise

The mean forcing of RCP8.5 by the year 2300 indicates that high-emissions scenarios overshoot both bifurcation and rate-induced thresholds of most AIS regions. Overshooting a critical forcing does not necessarily imply a collapse of the associated basin if it is followed by a sufficiently fast and substantial cooling[50]. However, this overshoot entails a risk of large SLR rates (Tables 1 and 2) and of up to 40–45 mSLE of committed SLR. This number might be an underestimate, because AIS equilibrium simulations have shown that including the albedo feedback, instead of a fixed conversion factor from GMT to regional anomalies, can trigger the total collapse of the AIS[7].

Although the warming scenarios used here are idealized, they have important implications for realistic SLR projections. When ice-sheet models are coupled to GIA models that do not account for the lateral variability of the solid Earth, the likelihood of triggering R-tipping via an emissions scenario is probably overestimated in the WAIS and underestimated in the EASBs. This supports the use of GIA models that resolve this lateral variability in continental-scale simulations of the AIS, especially because computationally efficient solutions have recently been proposed[36,51,52]. Furthermore, equilibrium diagrams of the AIS are sometimes obtained by running step experiments[7], although our experiments show that this maximizes the likelihood of R-tipping (Figs. 2 and 3) and can bias the bifurcation estimate.

To conclude, we show that the Recovery and Aurora subglacial basins are probably subject to R-tipping, even at forcing rates that are far smaller than those predicted in future emissions scenarios. As suggested by our simulations, the GIA response, although substantial in equilibrium, can be strongly delayed and therefore almost absent for rates as small as about 0.01 K per century. This delay results from the high mantle viscosities found in the Recovery and Aurora regions and eases the grounding zone migration into retrograde bed portions, which can trigger self-sustained retreats. Within ±2σ of the viscosity estimates, R-tipping can either be marginal or amount to a gap of 0.5 K GMT anomaly. This highlights the importance of better constraining the mantle viscosity of Antarctica to obtain more reliable SLR projections. Equally important, R-tipping is negligible in the WAIS and only marginal in the WSB, mostly due to the smaller GIA response before the onset of MISI and to locally lower mantle viscosities.

A natural way to continue this work is to investigate R-tipping for past ice sheets. For instance, the mantle viscosity in Hudson Bay and along the Kara Sea coast is larger than the global average[25,26] and could have led to R-tipping of the Laurentide and Eurasian ice sheets in the past.

Table 2 | Same as Table 1 but for the step forcing from 1.2 to 9 K of GMT anomaly

Region	ΔV (mSLE)	Δt_{core} (yr)	$\dot{s}_{mean}$ (mm yr^{-1})	$\dot{s}_{max}$ (mm yr^{-1})
WAIS	3.2	105	25.2	28.3
Wilkes	4.8	505	8.0	10.0
Recovery	1.9	325	5.3	5.7
Aurora ext.	1.4	370	3.7	4.0
Aurora int.	3.0	1,105	2.3	2.8

Online content

Any methods, additional references, Nature Portfolio reporting summaries, source data, extended data, supplementary information, acknowledgements, peer review information; details of author contributions and competing interests; and statements of data and code availability are available at https://doi.org/10.1038/s41561-026-02117-8.

References

1. Fretwell, P. et al. Bedmap2: improved ice bed, surface and thickness datasets for Antarctica. *Cryosphere* **7**, 375–393 (2013).
2. Morlighem, M. et al. Deep glacial troughs and stabilizing ridges unveiled beneath the margins of the Antarctic Ice Sheet. *Nat. Geosci.* **13**, 132–137 (2020).
3. Pritchard, H. D. et al. Bedmap3 updated ice bed, surface and thickness gridded datasets for Antarctica. *Sci. Data* **12**, 414 (2025).
4. Schoof, C. Ice sheet grounding line dynamics: steady states, stability, and hysteresis. *J. Geophys. Res.* **112**, F03S28 https://doi.org/10.1029/2006JF000664 (2007).
5. Weertman, J. Stability of the junction of an ice sheet and an ice shelf. *J. Glaciol.* **13**, 3–11 (1974).
6. Garbe, J., Albrecht, T., Levermann, A., Donges, J. & Winkelmann, R. The hysteresis of the Antarctic Ice Sheet. *Nature* **585**, 538–544 (2020).
7. Leloup, G., Quiquet, A., Roche, D. M., Dumas, C. & Paillard, D. Hysteresis of the Antarctic Ice Sheet with a coupled climate-ice-sheet model. *Geophys. Res. Lett.* **52**, e2024GL111492 (2025).
8. Winkelmann, R., Garbe, J., Donges, J. F. & Albrecht, T. Mapping tipping risks from Antarctic ice basins under global warming. *Nat. Clim. Change* **16**, 341–349 (2026).
9. Seroussi, H. et al. Evolution of the Antarctic Ice Sheet over the next three centuries from an ISMIP6 model ensemble. *Earth's Future* **12**, e2024EF004561 https://doi.org/10.1029/2024EF004561 (2024).
10. Coulon, V. et al. Disentangling the drivers of future Antarctic ice loss with a historically calibrated ice-sheet model. *Cryosphere* **18**, 653–681 (2024).
11. Coulon, V. et al. From short-term uncertainties to long-term certainties in the future evolution of the Antarctic Ice Sheet. *Nat. Commun.* **16**, 10385 (2025).
12. Houriez, L. et al. Reinforced ridges in Thwaites Glacier yield insights into resolution requirements for coupled ice sheet and solid Earth models. *Cryosphere* **19**, 4355–4372 https://doi.org/10.5194/tc-19-4355-2025 (2025).
13. Gudmundsson, G. H., Krug, J., Durand, G., Favier, L. & Gagliardini, O. The stability of grounding lines on retrograde slopes. *Cryosphere* **6**, 1497–1505 (2012).
14. Christianson, K. et al. Ice sheet grounding zone stabilization due to till compaction. *Geophys. Res. Lett.* **40**, 5406–5411 https://doi.org/10.1002/2013GL057447 (2013).
15. Sergienko, O. V. No general stability conditions for marine ice-sheet grounding lines in the presence of feedbacks. *Nat. Commun.* **13**, 2265 (2022).
16. Gomez, N., Mitrovica, J. X., Huybers, P. & Clark, P. U. Sea level as a stabilizing factor for marine-ice-sheet grounding lines. *Nat. Geosci.* **3**, 850–853 (2010).
17. Gomez, N., Pollard, D., Mitrovica, J. X., Huybers, P. & Clark, P. U. Evolution of a coupled marine ice sheet-sea level model. *J. Geophys. Res. Earth Surf.* **117**, F01013 https://doi.org/10.1029/2011JF002128 (2012).
18. Konrad, H. et al. The deformational response of a viscoelastic solid Earth model coupled to a thermomechanical ice sheet model. *Surv. Geophys.* **35**, 1441–1458 https://doi.org/10.1007/s10712-013-9257-8 (2014).
19. Konrad, H., Sasgen, I., Pollard, D. & Klemann, V. Potential of the solid-Earth response for limiting long-term West Antarctic Ice Sheet retreat in a warming climate. *Earth Planet. Sci. Lett.* **432**, 254–264 (2015).
20. Gomez, N., Latychev, K. & Pollard, D. A coupled ice sheet-sea level model incorporating 3D Earth structure: variations in Antarctica during the last deglacial retreat. *J. Clim.* **31**, 4041–4054 (2018).
21. Albrecht, T., Bagge, M. & Klemann, V. Feedback mechanisms controlling Antarctic glacial-cycle dynamics simulated with a coupled ice sheet-solid Earth model. *Cryosphere* **18**, 4233–4255 (2024).
22. Gomez, N. et al. The influence of realistic 3D mantle viscosity on Antarctica's contribution to future global sea levels. *Sci. Adv.* **10**, eadn1470 https://doi.org/10.1126/sciadv.adn1470 (2024).
23. van Calcar, C. J., Bernales, J., Berends, C. J., van der Wal, W. & van de Wal, R. S. W. Bedrock uplift reduces Antarctic sea-level contribution over next centuries. *Nat. Commun.* **16**, 10512 (2025).
24. Morelli, A. & Danesi, S. Seismological imaging of the Antarctic continental lithosphere: a review. *Glob. Planet. Change* **42**, 155–165 (2004).
25. Austermann, J., Hoggard, M. J., Latychev, K., Richards, F. D. & Mitrovica, J. X. The effect of lateral variations in Earth structure on last interglacial sea level. *Geophys. J. Int.* **227**, 1938–1960 (2021).
26. Bagge, M., Klemann, V., Steinberger, B., Latinović, M. & Thomas, M. Glacial-isostatic adjustment models using geodynamically constrained 3D Earth structures. *Geochem. Geophys. Geosyst.* **22**, e2021GC009853 https://doi.org/10.1029/2021GC009853 (2021).
27. Ivins, E. R., van der Wal, W., Wiens, D. A., Lloyd, A. J. & Caron, L. Antarctic upper mantle rheology. *Geol. Soc. London Mem.* **56**, M56–2020–19 https://doi.org/10.1144/M56-2020-19 (2022).
28. Hazzard, J. A. N. & Richards, F. D. Antarctic geothermal heat flow, crustal conductivity and heat production inferred from seismological data. *Geophys. Res. Lett.* **51**, e2023GL106274 https://doi.org/10.1029/2023GL106274 (2024).
29. Siteur, K., Eppinga, M. B., Doelman, A., Siero, E. & Rietkerk, M. Ecosystems off track: rate-induced critical transitions in ecological models. *Oikos* **125**, 1689–1699 https://doi.org/10.1111/oik.03112 (2016).
30. Ashwin, P., Wieczorek, S., Vitolo, R. & Cox, P. Tipping points in open systems: bifurcation, noise-induced and rate-dependent examples in the climate system. *Philos. Trans. R. Soc. A* **370**, 1166–1184 https://doi.org/10.1098/rsta.2011.0306 (2012).
31. Kaufman, D. S. & McKay, N. P. Technical note: past and future warming – direct comparison on multi-century timescales. *Clim. Past* **18**, 911–917 (2022).
32. Alkhayuon, H., Ashwin, P., Jackson, L. C., Quinn, C. & Wood, R. A. Basin bifurcations, oscillatory instability and rate-induced thresholds for Atlantic meridional overturning circulation in a global oceanic box model. *Proc. R. Soc. A* **475**, 20190051 https://doi.org/10.1098/rspa.2019.0051 (2019).
33. Lohmann, J. & Ditlevsen, P. D. Risk of tipping the overturning circulation due to increasing rates of ice melt. *Proc. Natl Acad. Sci. USA* **118**, e2017989118 https://doi.org/10.1073/pnas.2017989118 (2021).

34. Kypke, K. et al. Chaotic fluctuations in Greenland ice streams limit predictability of ice sheet collapse. *Earth Syst. Dyn.* **17**, 769–794 (2026).
35. Robinson, A. et al. Description and validation of the ice-sheet model Yelmo (version 1.0). *Geosci. Model Dev.* **13**, 2805–2823 (2020).
36. Swierczek-Jereczek, J. et al. FastIsostasy v1.0 – a regional, accelerated 2D glacial isostatic adjustment (GIA) model accounting for the lateral variability of the solid Earth. *Geosci. Model Dev.* **17**, 5263–5290 (2024).
37. The IMBIE team Mass balance of the Antarctic Ice Sheet from 1992 to 2017. *Nature* **558**, 219–222 (2018).
38. Swierczek-Jereczek, J., Alvarez-Solas, J., Robinson, A., Gutiérrez-González, L. & Montoya, M. Highlighting processes underlying the stability and hysteresis of the Antarctic Ice Sheet. Preprint at *EGUsphere* https://egusphere.copernicus.org/preprints/2026/egusphere-2025-6566/ (2026).
39. Collins, M. et al. Long-term climate change: projections, commitments and irreversibility. In *Climate Change 2013: The Physical Science Basis* (eds Stocker, T. et al.) 1029–1136 (Cambridge Univ. Press, 2013).
40. Barletta, V. R. et al. Observed rapid bedrock uplift in Amundsen Sea Embayment promotes ice-sheet stability. *Science* **360**, 1335–1339 https://doi.org/10.1126/science.aao1447 (2018).
41. Swierczek-Jereczek, J. et al. Fast approximation of Antarctica's GIA response to future ice melt with 3-D Earth structure. Preprint at *EGUsphere* https://egusphere.copernicus.org/preprints/2026/egusphere-2026-2640/ (2026).
42. Williams, C. R. et al. Calculations of extreme sea level rise scenarios are strongly dependent on ice sheet model resolution. *Commun. Earth Environ.* **6**, 60 (2025).
43. Jones, C. et al. The TIPMIP Earth system model experiment protocol: phase 1. *Geosci. Model Dev.* **19**, 6941–6966 https://doi.org/10.5194/gmd-19-6941-2026 (2025).
44. Ashwin, P., Perryman, C. & Wieczorek, S. Parameter shifts for nonautonomous systems in low dimension: bifurcation- and rate-induced tipping. *Nonlinearity* **30**, 2185–2210 (2017).
45. Swierczek-Jereczek, J., Robinson, A., Blasco, J., Alvarez-Solas, J. & Montoya, M. Time-scale synchronisation of oscillatory responses can lead to non-monotonous R-tipping. *Sci. Rep.* **13**, 2104 (2023).
46. MacAyeal, D. R. Irregular oscillations of the West Antarctic Ice Sheet. *Nature* **359**, 29–32 (1992).
47. MacAyeal, D. R. Binge/purge oscillations of the Laurentide Ice Sheet as a cause of the North Atlantic's Heinrich events. *Paleoceanography* **8**, 775–784 https://doi.org/10.1029/93PA02200 (1993).
48. Zeitz, M., Haacker, J. M., Donges, J. F., Albrecht, T. & Winkelmann, R. Dynamic regimes of the Greenland Ice Sheet emerging from interacting melt-elevation and glacial isostatic adjustment feedbacks. *Earth Syst. Dyn.* **13**, 1077–1096 (2022).
49. Golledge, N. R. et al. State dependent ice-sheet resonance under Cenozoic and future climates. *Commun. Earth Environ.* **7**, 114 (2026).
50. Bochow, N. et al. Overshooting the critical threshold for the Greenland ice sheet. *Nature* **622**, 528–536 (2023).
51. Coulon, V. et al. Contrasting response of West and East Antarctic ice sheets to glacial isostatic adjustment. *J. Geophys. Res. Earth Surf.* **126**, e2020JF006003 https://doi.org/10.1029/2020JF006003 (2021).
52. van Calcar, C. J., Whitehouse, P. L., van de Wal, R. S. W. & van der Wal, W. Approximating 3D bedrock deformation in an Antarctic ice-sheet model for projections. *Cryosphere* **20**, 757–775 (2026).
53. Schaffer, J. et al. A global, high-resolution data set of ice sheet topography, cavity geometry, and ocean bathymetry. *Earth Syst. Sci. Data* **8**, 543–557 (2016).

Publisher's note Springer Nature remains neutral with regard to jurisdictional claims in published maps and institutional affiliations.

Open Access This article is licensed under a Creative Commons Attribution-NonCommercial-NoDerivatives 4.0 International License, which permits any non-commercial use, sharing, distribution and reproduction in any medium or format, as long as you give appropriate credit to the original author(s) and the source, provide a link to the Creative Commons licence, and indicate if you modified the licensed material. You do not have permission under this licence to share adapted material derived from this article or parts of it. The images or other third party material in this article are included in the article's Creative Commons licence, unless indicated otherwise in a credit line to the material. If material is not included in the article's Creative Commons licence and your intended use is not permitted by statutory regulation or exceeds the permitted use, you will need to obtain permission directly from the copyright holder. To view a copy of this licence, visit http://creativecommons.org/licenses/by-nc-nd/4.0/.

© The Author(s) 2026

Methods

Yelmo

Yelmo is a thermo-mechanically coupled 3D ice-sheet model[35] that uses the depth-integrated velocity approximation[54] to solve the ice dynamics. The simulations are performed on a regular grid covering Antarctica with a horizontal resolution of $\Delta x = \Delta y = 16$ km and a vertical resolution of ten quadratically scaled layers, ranging from $\Delta z \simeq 0.01 \cdot H$ at the base up to $\Delta z \simeq 0.4 \cdot H$ at the top. This is defined as a fraction of the ice thickness, H, due to the sigma-transform applied to the vertical dimension. The ice dynamics follows a Glen flow law with exponent $n = 3$ and enhancement factors of 1.0, 1.0 and 0.7 for the shear, stream and shelf regions, respectively. At the grounding zone, a tidal partial melt parameterization is applied to include the effect of water intrusion through tides[55]. Calving is parameterized through a von Mises–type criterion[56], basal hydrology follows from a local energy balance and a fixed till drainage rate[57], and basal friction follows a regularized Coulomb law[58]. Finally, the unknown basal friction coefficient field is inferred by inversion of the present-day ice thickness and ice velocity. The resulting root-mean-square errors in ice surface elevation and velocity are 114 m and 96 m yr^{-1}, respectively. Both of these values lie within the range of the ISMIP6 models[9].

Forcing

The GMT anomaly is converted into a regional atmospheric temperature anomaly by using a fixed factor of 1.8, as assessed for Antarctica in the Polar Amplification Model Intercomparison Project[59]. This anomaly is uniformly added to the surface air temperature field of the 2023 climatology produced by the Regional Atmospheric Climate Model (RACMO2.3) (ref. 60). As the ice topography changes over time, the surface air temperature is modified according to a lapse rate of −6.5 K km^{-1}. The precipitation anomaly is computed through a fixed 5% K^{-1} factor (accounting for regional warming and elevation changes), and the surface melt is calculated with the positive degree-day method[61]. In an ensemble of long-term CMIP5 and CMIP6 simulations, the warming of the Southern Ocean was assessed to be about 25% of the regional atmospheric warming[62]. We therefore compute the regional oceanic temperature anomaly by scaling the atmospheric one with 0.25. This anomaly is uniformly added to the present-day ocean temperature field provided by ISMIP6 (refs. 63,64) and is subsequently converted into sub-shelf melting via a quadratic non-local law[65].

FastIsostasy

Yelmo is coupled to FastIsostasy, a regional GIA model that accounts for the lateral variability of the lithospheric thickness and the upper-mantle viscosity in the computation of the vertical bedrock displacement. Additionally, it approximates the changes in sea-surface elevation resulting from the redistribution of mass. This offers a computationally efficient alternative to 3D GIA models, without substantial loss of accuracy[36]. Nonetheless, FastIsostasy is subject to limitations: it underestimates the peripheral forebulge, ignores the rotational feedback, parameterizes the depth dependence of the viscosity and relies on a Maxwell rheology. The first two aspects are rather irrelevant here. The third one is addressed by calibrating the conversion of the 3D viscosity to a 2D one to minimize the error of FastIsostasy compared with a 3D GIA model on a large-scale collapse of the AIS[41]. Finally, the use of a Burgers rheology is the only increase in complexity that could alter the timescale separation between the ice retreat and the GIA response. Investigating this is left for future work.

Analysis of SLR rates

Whereas the total SLR associated with a bifurcation is the relevant metric for long-term impacts (for example, equilibrium coastline positions), the SLR rate is more informative when it comes to designing efficient adaptation strategies. To this end, we derive several key metrics for the five largest bifurcations: ΔV, the total loss of ice volume above flotation; Δt, the time span over which the bulk of this transition occurs; $\dot{s}_{\mathrm{mean}}$ and $\dot{s}_{\mathrm{max}}$, the mean and maximum SLR rates simulated over this time span. Computing these metrics for all experiments would yield results that are difficult to analyse; we therefore consider the quasi-equilibrium case first, for which the results are summarized in Table 1.

Depending on the basin, the autonomous collapse can last from about 5 kyr (WAIS) to about 12 kyr (Recovery). This timescale seems to be set by the bathymetry, which presents a very open shape, strong retrograde slopes and only a few large-scale pinning points in the WAIS. In contrast, the bathymetry presents narrow ocean channels with large pinning points in the RSB (Fig. 4). The volume, divided by the timescale of collapse, yields the mean autonomous SLR rate, which ranges from 0.1 (RSB) to 0.5 mm yr^{-1} (WAIS). Similarly, the maximum SLR rate ranges from 0.4 (external ASB) to 1.8 mm yr^{-1} (WAIS). Altogether, this shows a considerable heterogeneity of autonomous SLR rates among the basins, meaning that their collapses have different implications for adaptation strategies.

The autonomous metrics are of key interest because they reflect an intrinsic property of the modelled ice sheet. However, in realistic warming scenarios, the GMT typically increases monotonically until the year 2300. Therefore, the autonomous SLR rates only represent lower bounds. To give upper bounds for transient runs, we analyse the results of a step experiment with a GMT anomaly of 9 K, summarized in Table 2. For this case, the mean and maximum SLR rates are typically increased by more than an order of magnitude. The maximum values arise for the WAIS, which reaches a mean SLR rate of 25.2 mm yr^{-1}—about half of the reconstructed SLR rates associated with meltwater pulse 1A (MWP1A)[66]. Recovery and Aurora, both subject to R-tipping, show maximum SLR rates of up to 5.7 and 2.8 mm yr^{-1}, respectively. In comparison, the average Antarctic contribution to SLR over the 1992–2017 period is only 0.4 mm yr^{-1} (ref. 37).

It is worth noting that the bounds on SLR rates that are inferred here are conservative because they are derived from extreme scenarios (zero versus infinite forcing rate). Furthermore, they are intrinsically linked to model limitations: to obtain more reliable values, substantial development efforts are needed. In particular, ice–ocean interactions largely determine the evolution of marine-based regions, yet their representation in numerical ice-sheet models remains to be substantially improved. Therefore, the numbers in Tables 1 and 2 are indicative, intentionally conservative and by no means a final assessment.

Data availability

A reduced version of the output data, sufficient to reproduce all figures presented in the paper, is available via Zenodo at https://doi.org/10.5281/zenodo.21935199 (ref. 67). This includes the parameters of the solid-Earth structure, the observational dataset used for comparison in Extended Data Fig. 1, the time series of all ramp and step experiments, the spatio-temporal output of the experiments illustrated in the paper, and both time series and spatio-temporal output of the quasi-equilibrium experiments. Additional output can be made available upon request.

Code availability

The code used to generate the figures shown here is available via Github at https://github.com/JanJereczek/rtip-ais. The source code of Yelmo and FastIsostasy can be accessed via Github at https://github.com/palma-ice/yelmo and https://github.com/palma-ice/FastIsostasy, respectively.

References

54. Robinson, A., Goldberg, D. & Lipscomb, W. H. A comparison of the stability and performance of depth-integrated ice-dynamics solvers. *Cryosphere* **16**, 689–709 (2022).

55. Juarez-Martinez, A. et al. Parameterizing tidal-water intrusions in long-term Antarctic ice-sheet projections. Preprint at *EGUsphere* https://egusphere.copernicus.org/preprints/2026/egusphere-2026-248/ (2026).
56. Lipscomb, W. H. et al. Description and evaluation of the Community Ice Sheet Model (CISM) v2.1. *Geosci. Model Dev.* **12**, 387–424 (2019).
57. Bueler, E. & van Pelt, W. Mass-conserving subglacial hydrology in the Parallel Ice Sheet Model version 0.6. *Geosci. Model Dev.* **8**, 1613–1635 (2015).
58. Zoet, L. K. & Iverson, N. R. A slip law for glaciers on deformable beds. *Science* **368**, 76–78 https://doi.org/10.1126/science.aaz1183 (2020).
59. Smith, D. M. et al. The Polar Amplification Model Intercomparison Project (PAMIP) contribution to CMIP6: investigating the causes and consequences of polar amplification. *Geosci. Model Dev.* **12**, 1139–1164 (2019).
60. Van Wessem, J. M., Van De Berg, W. J. & Van Den Broeke, M. R. Data set: monthly averaged RACMO2.3p2 variables; Antarctica. *Zenodo* https://doi.org/10.5281/zenodo.7760491 (2023).
61. Reeh, N. in *Quaternary Geology of Canada and Greenland* Vol. K-1 (ed. Fulton, R. J.) Ch. 14 https://doi.org/10.1130/DNAG-GNA-K1.793 (Geological Society of America, 1989).
62. Golledge, N. R. et al. The multi-millennial Antarctic commitment to future sea-level rise. *Nature* **526**, 421–425 (2015).
63. Jourdain, N. C. et al. A protocol for calculating basal melt rates in the ISMIP6 Antarctic Ice Sheet projections. *Cryosphere* **14**, 3111–3134 (2020).
64. Seroussi, H. et al. ISMIP6 Antarctica: a multi-model ensemble of the Antarctic Ice Sheet evolution over the 21st century. *Cryosphere* **14**, 3033–3070 (2020).
65. Favier, L. et al. Assessment of sub-shelf melting parameterisations using the ocean-ice-sheet coupled model NEMO(v3.6)-Elmer/Ice(v8.3). *Geosci. Model Dev.* **12**, 2255–2283 (2019).
66. Lambeck, K., Rouby, H., Purcell, A., Sun, Y. & Sambridge, M. Sea level and global ice volumes from the Last Glacial Maximum to the Holocene. *Proc. Natl Acad. Sci. USA* **111**, 15296–15303 (2014).
67. Swierczek-Jereczek, J., Blasco Navarro, J., Robinson, A., Alvarez Solas, J. & Montoya, M. Supporting data of rate-induced tipping of the Antarctic Ice Sheet controlled by solid-Earth feedbacks by Swierczek-Jereczek et al. *Zenodo* https://doi.org/10.5281/zenodo.21935199 (2026).
68. Rignot, E., Mouginot, J. & Scheuchl, B. Ice flow of the Antarctic Ice Sheet. *Science* **333**, 1427–1430 https://doi.org/10.1126/science.1208336 (2011).

Acknowledgements

J.S.-J. thanks T. Albrecht and P. Ashwin for helpful discussions. J.S.-J. also thanks the PhD students of the Department of Earth Physics and Astrophysics for their everyday support.

Author contributions

J.S.-J., M.M., J.A.-S. and A.R. designed the study. J.S.-J. and A.R. coupled Yelmo to FastIsostasy. J.S.-J., J.B. and J.A.-S. performed the model calibration. J.S.-J. conducted the experiments and wrote the paper, with input from all co-authors.

Funding

J.S.-J. and J.B. received funding from the EU H2020 research infrastructures of the European Commission (CriticalEarth, grant number 956170 and ClimTip, grant number 101137601). This is ClimTip contribution number 69. A.R. received funding from the European Research Council (ERC Consolidator grant, FORCLIMA, grant number 101044247). M.M. and J.A.-S. received funding from the Spanish Ministry of Science, Innovation and Universities (project CREEP, grant number PID2024-156476OB-I00; project CCRYTICAS, grant number PID2022-142800OB-I00).

Competing interests

The authors declare no competing interests.

Additional information

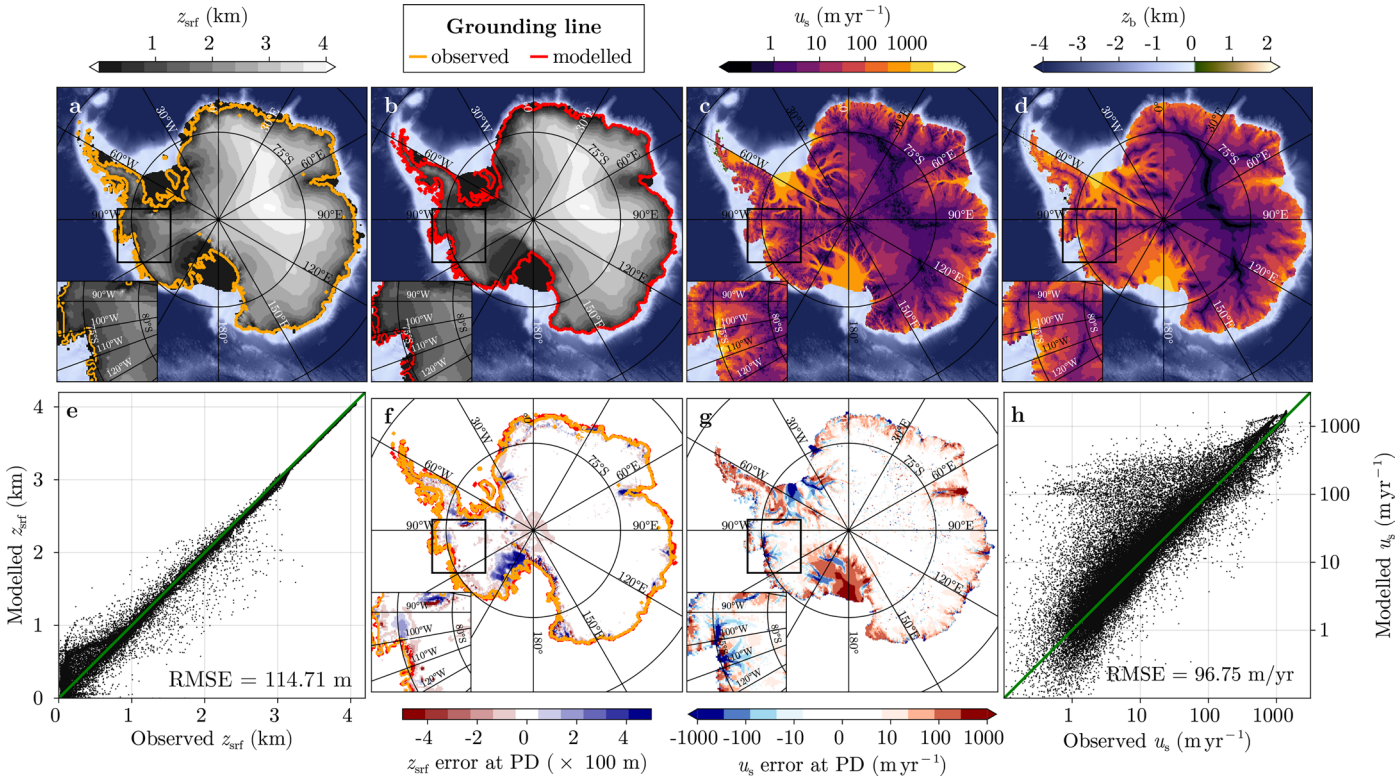
Extended data is available for this paper at https://doi.org/10.1038/s41561-026-02117-8.

Correspondence and requests for materials should be addressed to Jan Swierczek-Jereczek or Jorge Alvarez-Solas.

Peer Review Information *Nature Geoscience* thanks Surendra Adhikari, Fuyuki Saito and the other, anonymous, reviewer for their contribution to the peer review of this work. Primary Handling Editors: Tamara Goldin and Aliénor Lavergne, in collaboration with the *Nature Geoscience* team.

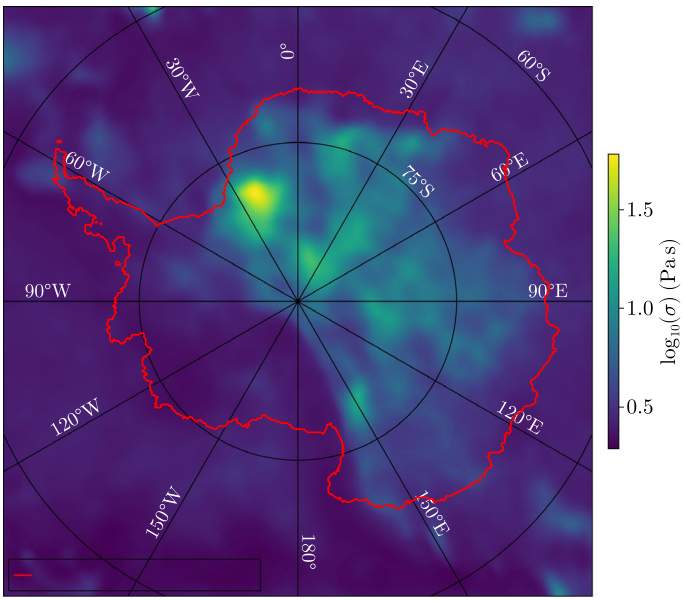
Reprints and permissions information is available at www.nature.com/reprints.

https://doi.org/10.1038/s41561-026-02117-8



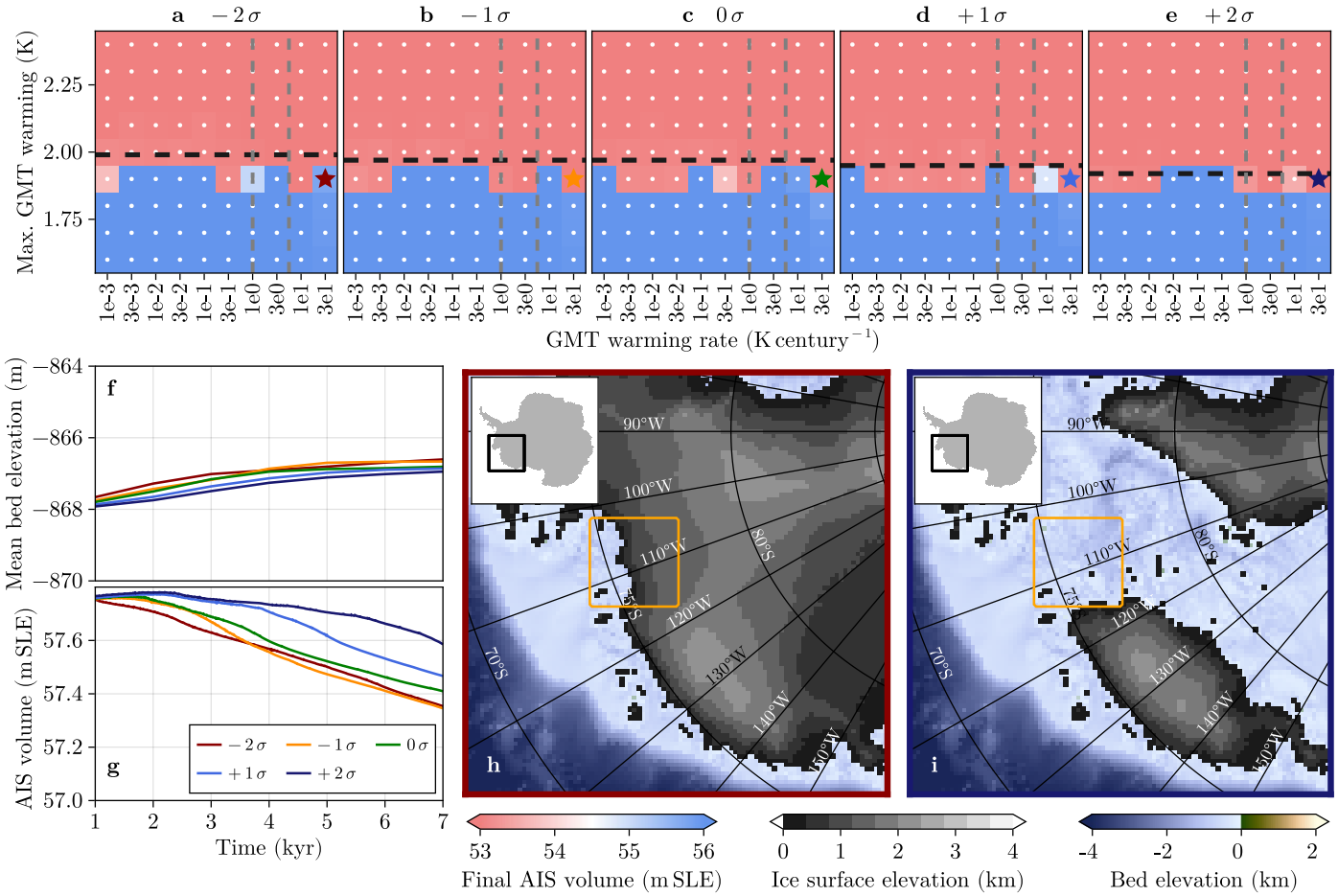
Extended Data Fig. 1 | Present-day error metrics of the simulated AIS. (**a**) Observed [53] and (**b**) modelled ice surface elevation at the present day. (**c**) Observed [68] and (**d**) modelled ice surface velocity at the present day. (**e** & **h**) Error plots of the ice surface elevation and velocity (modelled value against observed one). (**f** & **g**) Error maps of the ice surface elevation and velocity (modelled value minus observed one).

https://doi.org/10.1038/s41561-026-02117-8



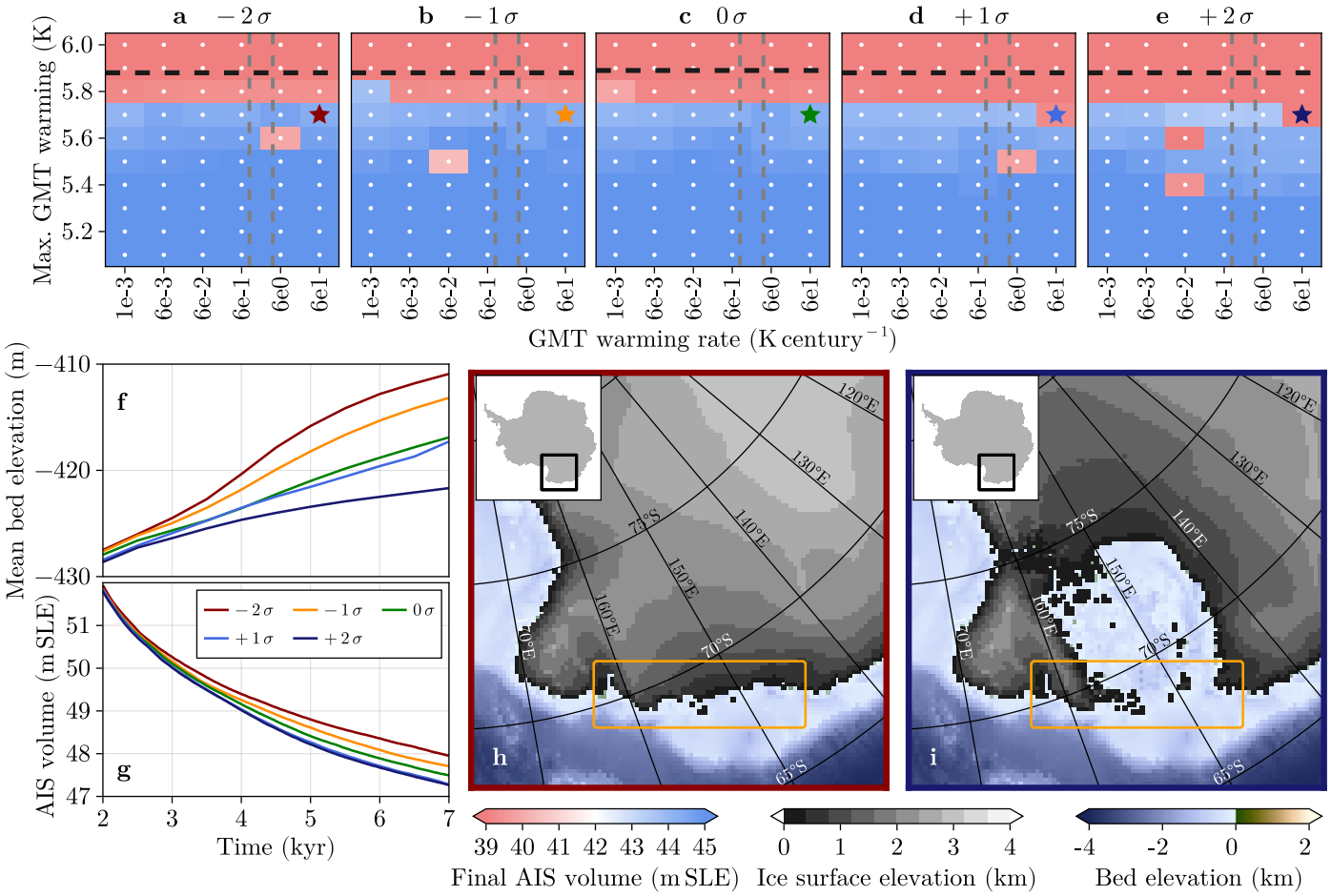
Extended Data Fig. 2 | Standard deviation of the viscosity estimate. We here show the averaged value between the bottom of the lithosphere and a standard depth of 350 km [28]. Since lumping the 3D viscosity into a 2D effective one is a nonlinear procedure, the $\pm 2\,\sigma$ cases are not symmetric and are therefore separately plotted in Fig. 1.

https://doi.org/10.1038/s41561-026-02117-8



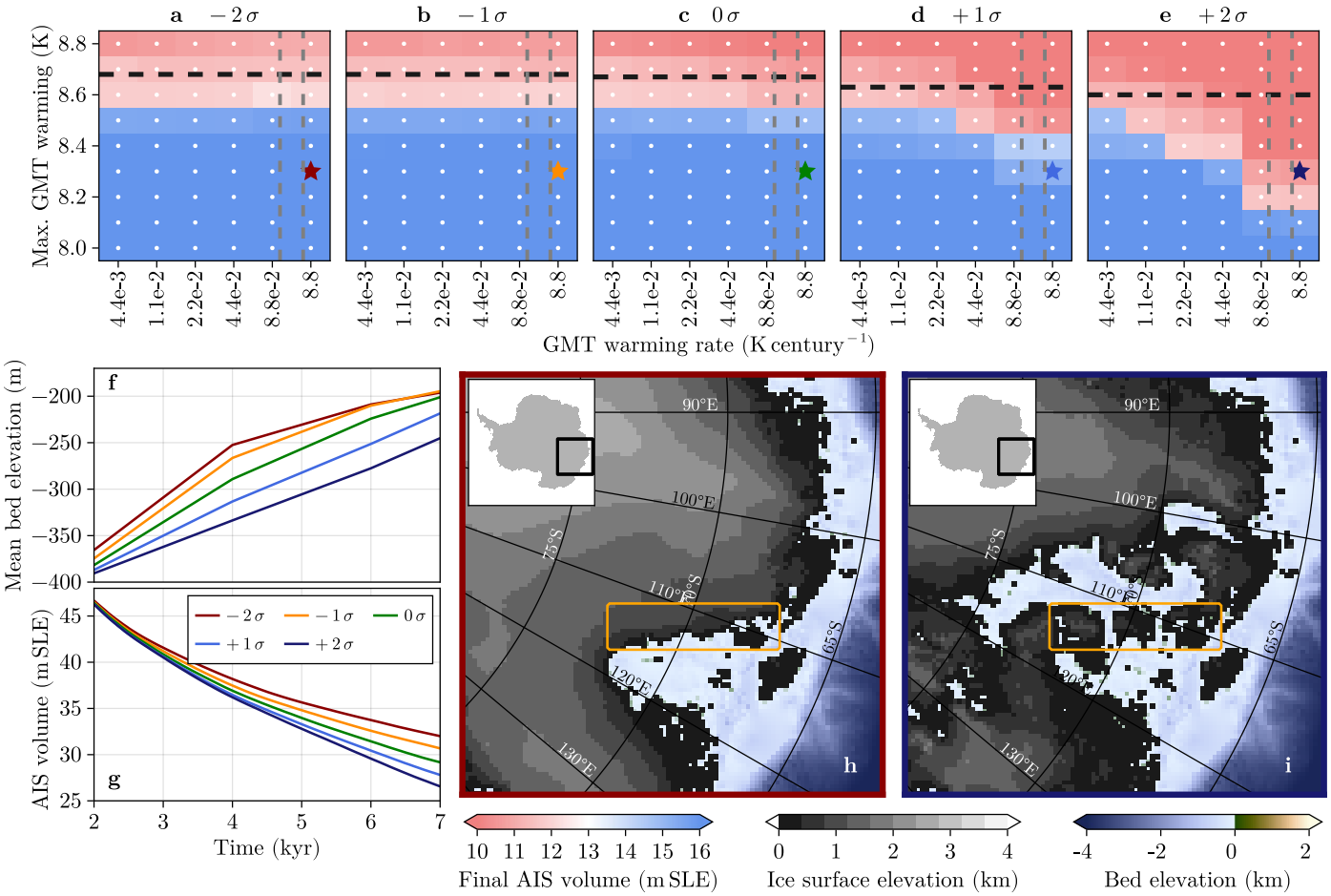
Extended Data Fig. 3 | R-tipping diagram of the WAIS. (**a**-**e**) Final AIS volume above flotation as a function of the maximal rate and amplitude of GMT anomaly, for the five upper-mantle viscosity cases. The existence of a bifurcation is responsible for the binary behaviour of the final equilibrium AIS volume. The dashed horizontal line represents the bifurcation point of the WAIS and each white dot corresponds to a ramp simulation. The vertical lines represent the mean rate of warming since the pre-industrial era and the highest rate projected until 2300 under RCP8.5. (**f**-**g**) Mean bed elevation over the region of interest and AIS volume time series corresponding to the star markers in (**a**-**e**). (**h**-**i**) Final WAIS configuration for the low (red star in panel **a**) and high (blue star in panel **e**) viscosity cases with the same ramp forcing. The region of interest is delimited by the orange rectangle.

https://doi.org/10.1038/s41561-026-02117-8



Extended Data Fig. 4 | R-tipping diagram of the WSB. (**a**-**e**) Final AIS volume above flotation as a function of the maximal rate and amplitude of GMT anomaly, for the five upper-mantle viscosity cases. The existence of a bifurcation is responsible for the binary behaviour of the final equilibrium AIS volume. The dashed horizontal line represents the bifurcation point of the WSB and each white dot corresponds to a ramp simulation. The vertical lines represent the mean rate of warming since the pre-industrial era and the highest rate projected until 2300 under RCP8.5. (**f**-**g**) Mean bed elevation over the region of interest and AIS volume time series corresponding to the star markers in (**a**-**e**). (**h**-**i**) Final WSB configuration for the low (red star in panel **a**) and high (blue star in panel **e**) viscosity cases with the same ramp forcing. The region of interest is delimited by the orange rectangle.

https://doi.org/10.1038/s41561-026-02117-8



Extended Data Fig. 5 | R-tipping diagram of the ASB. (**a**-**e**) Final AIS volume above flotation as a function of the maximal rate and amplitude of GMT anomaly, for the five upper-mantle viscosity cases. The existence of a bifurcation is responsible for the binary behaviour of the final equilibrium AIS volume. The dashed horizontal line represents the bifurcation point of the ASB and each white dot corresponds to a ramp simulation. The vertical lines represent the mean rate of warming since the pre-industrial era and the highest rate projected until 2300 under RCP8.5. (**f**-**g**) Mean bed elevation over the region of interest and AIS volume time series corresponding to the star markers in (**a**-**e**). (**h**-**i**) Final ASB configuration for the low (red star in panel **a**) and high (blue star in panel **e**) viscosity cases with the same ramp forcing. The region of interest is delimited by the orange rectangle.